

Detection of the Cosmic Infrared Background at 2.2 and 3.5 μm Using DIRBE Observations

E. L. Wright

Department of Physics and Astronomy, University of California, Los Angeles, CA 90095-1562

wright@astro.ucla.edu

and

E. D. Reese

Department of Astronomy & Astrophysics, University of Chicago, 5640 S. Ellis Ave., Chicago, IL 60637

reese@piglet.uchicago.edu

ABSTRACT

We compare data from the Diffuse InfraRed Background Experiment (DIRBE) on the Cosmic Background Explorer (*COBE*) satellite to the the Wainscoat *et al.* (1992) model of the infrared sky. The model is first compared with broadband *K* (2.2 μm) star counts. Its success at *K*-band gives credence to its physical approach which is extrapolated to the *L*-band (3.5 μm). We have analyzed the histograms of the pixel by pixel intensities in the 2.2 and 3.5 μm maps from DIRBE after subtracting the zodiacal light. The shape of these histograms agrees quite well with the histogram shape predicted using the Wainscoat *et al.* (1992) model of the infrared sky, but the predicted histograms must be displaced by a constant intensity in order to match the data. This shift is the cosmic infrared background, which is $16.9 \pm 4.4 \text{ kJy sr}^{-1}$ or $23.1 \pm 5.9 \text{ nW m}^{-2} \text{ sr}^{-1}$ at 2.2 μm , and $14.4 \pm 3.7 \text{ kJy sr}^{-1}$ or $12.4 \pm 3.2 \text{ nW m}^{-2} \text{ sr}^{-1}$ at 3.5 μm .

Subject headings: cosmology: observations — diffuse radiation — infrared:general

1. Introduction

Theoretical consideration of the cosmic infrared background (CIRB) radiation began decades ago with a paper by Partridge & Peebles (1967). It took quite some time for the IR detector technology to catch up to the sensitivity demands in detecting the faint CIRB. The Diffuse InfraRed Background Experiment (DIRBE) on the Cosmic Background Explorer (*COBE*) is designed specifically to detect the CIRB. The DIRBE team reported detections of the CIRB at 140 and 240 μm ,

and upper limits at other wavelengths from 1.25 to 100 μm , in Hauser *et al.* (1998), Kelsall *et al.* (1998) and Arendt *et al.* (1998). Dwek & Arendt (1998) reported a *lower limit* at 3.5 μm based on the correlation between the 2.2 and 3.5 μm DIRBE maps and a lower limit at 2.2 μm based on galaxy counts. Gorjian, Wright & Chary (2000) have reported a tentative detection of the CIRB at both 2.2 and 3.5 μm after directly measuring and subtracting the galactic stars in a “dark spot”.

The main source of the CIRB is thought to be the superimposed light of distant galaxies. The optical and UV radiation emitted from early star formation in such galaxies is red shifted to the NEAR INFRARED (NIR) in the present epoch. The observation of the CIRB is complicated by local contributors to the NIR flux: scattering and thermal re-emission from interplanetary dust (IPD), known as zodiacal light (ZL); the interstellar medium (ISM) in the Milky Way; and foreground stars in our own galaxy. Extragalactic sources include pregalactic stars, cosmic explosions, and possibly decaying elementary particles if they attain a sufficient density. *Due to these sources*, the CIRB offers information regarding the nature and evolution of early luminous matter, be it stars or primeval galaxies; limits on the epoch of galaxy formation; the presence or absence of dust in early galaxies; and constraints on the reheating of the universe between $z = 5$ and 10^3 (Fukugita & Kawasaki 1993). There is a minimum in IPD flux and zodiacal light at 3.5 μm (see Figure 1 of Carr (1992)) creating a ‘window’ for observing the CIRB. The regions away from the galactic plane offer the lowest star density, and thus low contaminating stellar flux, plus minimal dust obscuration from our own galaxy.

In this paper we first remove the strong zodiacal light foreground and the small interstellar medium foreground from the DIRBE maps at 2.2 & 3.5 μm . The maps after these subtractions are very strongly confusion limited by the overlapping signals from galactic stars. We have modeled the histogram of pixel values using a modified version of the Wainscoat *et al.* (1992, hereafter WCVWS) IR model of the Galaxy to predict star counts at 2.2 & 3.5 μm , after testing the model against actual observations in several parts of the Galaxy at 2.2 μm . The model histograms match the observed histograms very well after a constant offset is added to the model, and this offset is the value of the CIRB.

2. Foregrounds

2.1. Zodiacal Light

Kelsall *et al.* (1998) describe the zodiacal light model used by Hauser *et al.* (1998). But Kelsall *et al.* (1998) leave a large residual intensity in the galactic polar caps at 25 μm , the DIRBE band that is most dominated by the zodiacal light. For example, the 25 μm intensity toward the DIRBE dark spot at $(l, b) = (120.8^\circ, 65.9^\circ)$ in the DIRBE ZSMA (Zodi Subtracted Mission Average) maps prepared using the Kelsall *et al.* (1998) model is 1.76 MJy sr^{-1} . This cannot be a cosmic background because the lack of γ -ray emission toward Mkn 501 limits the CIRB to be < 33 kJy sr^{-1} (Funk *et al.* 1998). It also cannot be a galactic signal because the 100 μm intensity in

this field is 1.27 MJy sr^{-1} in the ZSMA maps, and Arendt *et al.* (1998) specify the ISM intensity as $R(\lambda)(I(100) - I_o)$, with the ratio of $25 \mu\text{m}$ to $100 \mu\text{m}$ galactic signals (in MJy sr^{-1}) given by $R(25) = 0.0480$, and the $100 \mu\text{m}$ intensity extrapolated to zero N_H is $I_o = 0.66 \text{ MJy sr}^{-1}$, so the ISM intensity at $25 \mu\text{m}$ is only 29 kJy sr^{-1} . By elimination, most of this intensity must be zodiacal.

In order to reduce the residual zodiacal emission in the maps, Wright (1997) added one “observation” that the high b intensity at $25 \mu\text{m}$ should be zero to the more than 10^5 observations used in the zodiacal model fitting. Even this very low weight pseudo-observation lowered the $25 \mu\text{m}$ intensity in the dark spot to 0.26 MJy sr^{-1} . This indicates that the isotropic component of the zodiacal emission is very poorly constrained in fits that just look at the time variation to measure the zodiacal light. The Appendix in Wright (1998) discusses zodiacal light models in more depth, and Gorjian *et al.* (2000) give the actual parameters of the model we have used.

Since the residual $25 \mu\text{m}$ intensity is now only 1% of the total zodiacal emission, we might hope for errors in the ZL model equal to 1% of the ecliptic pole intensity. But the situation is more uncertain at 2.2 and $3.5 \mu\text{m}$ due to the scattered component of the ZL. Adjusting the thermal emission component to fit the $25 \mu\text{m}$ intensity will not necessarily lead to a correct scattered component. So we have adopted ZL modeling errors of 5% of the intensity at the ecliptic poles at 2.2 and $3.5 \mu\text{m}$. These errors are slightly lower at $2.2 \mu\text{m}$ (5.2 vs. $6 \text{ nW m}^{-2} \text{ sr}^{-1}$) and higher at $3.5 \mu\text{m}$ (2.8 vs. $2 \text{ nW m}^{-2} \text{ sr}^{-1}$) than the errors adopted by Kelsall *et al.* (1998).

2.2. Interstellar Medium

Arendt *et al.* (1998) give a method for removing interstellar medium emission from the maps after the zodiacal light is removed. The corrected map is given by

$$I'_\nu(\lambda) = I_\nu(\lambda) - R(\lambda)(I_\nu(100) - I_o) \quad (1)$$

where the intensity ratio $R(3.5) = 0.00183$ but $R(2.2) = 0$. I_o is the intercept at zero N_H of the zodi-subtracted $100 \mu\text{m}$ map. Thus I_o is an intensity that is not from the solar system and not from the Galaxy. In the Arendt *et al.* (1998) analysis it is assumed to be a cosmic background, but Hauser *et al.* (1998) do not claim a detection of a cosmic background at $100 \mu\text{m}$ because of the uncertainties in the analysis that leads to I_o . Arendt *et al.* (1998) give the value $I_o = 19.8 \pm 2.5 \text{ nW m}^{-2} \text{ sr}^{-1}$, or 660 kJy sr^{-1} .

In our analysis we have used a map of $I_\nu(3.5) - R(3.5)I_\nu(100)$. Comparing this to the Arendt *et al.* (1998) formula shows that we need to add $R(\lambda)I_o$ to our final result because we have over-subtracted the interstellar medium in our maps. But we should not use the $I_o = 0.66 \text{ MJy sr}^{-1}$ of Arendt *et al.* (1998) because we have subtracted more zodiacal light than the Kelsall *et al.* (1998) model, and this will lower the zero N_H intercept in the zodi-subtracted $100 \mu\text{m}$ map. The difference in the zodiacal light model averages to 0.3 MJy sr^{-1} in the regions we study in this paper, so we use $I_o = 0.4 \text{ MJy sr}^{-1}$, and add 0.7 kJy sr^{-1} to our $3.5 \mu\text{m}$ results. No correction is needed at 2.2

μm .

3. The Starcount Model

Star count calculations used a modified version of the WCVWS starcount model which incorporates the spiral arm modifications made by Cohen (1994). Except for recoding and a different treatment of the Gaussian distribution of absolute magnitudes, our starcount model is the same as that used by Arendt *et al.* (1998) for computing their Faint Source Model. The model breaks the galaxy into five components: disk, spiral arms, molecular ring, central bulge, and extended halo. Integration is performed along the line of sight extending from the Sun to the desired galactic longitude and latitude through each galactic component. Each component is populated by 87 different stellar types distributed among the five galactic components using a weighting technique to simulate the distribution observed in the Galaxy. The spectral classes are characterized by absolute magnitudes in various IR wavelengths, a magnitude dispersion, z -component disk scale height (z is the height above the galactic plane), solar neighborhood density, and relative weights for each galactic component. Dust is modeled with a smooth exponential distribution following the Rieke & Lebofsky (1985) extinction law. The model is able to perform calculations in the J , K , L , and M bands and at 12 and 25 μm .

3.1. Components of the model

The differential star counts are given by

$$\begin{aligned} \frac{dN}{dm}(m) &= \int_0^S \left\{ \sum_{i=1}^{87} \rho_o^i [\exp(-|z|/h_z^i) (D(\vec{r}) \{f_D^i + f_A^i A(\vec{r})\} + f_R^i \mathcal{R}(\vec{r}) + f_B^i B(\vec{r}) + f_H^i H(\vec{r})) \right. \\ &\times \left. \frac{\exp[-(M_\lambda^i + 5 \log(s/10 \text{ pc}) + A_\lambda(\vec{r}) - m)^2 / (2\sigma_i^2)]}{\sigma_i \sqrt{2\pi}} \right\} s^2 ds \end{aligned} \quad (2)$$

where the spatial components for the disk, $D(\vec{r})$; spiral arms, $A(\vec{r})$; molecular ring, $\mathcal{R}(\vec{r})$; bulge, $B(\vec{r})$; halo, $H(\vec{r})$; and dust, $A_\lambda(\vec{r})$ are discussed in the following paragraphs. The weights f_D^i , f_A^i , f_R^i , f_B^i and f_H^i give the relative importance of the disk, arm, ring, bulge and halo spatial components for the i^{th} star type. The position along the line-of-sight is given by

$$\vec{r} = (x, y, z) = (-R_o + \cos(l) \cos(b)s, \sin(l) \cos(b)s, 18 \text{ pc} + \sin(b)s). \quad (3)$$

We use an offset of the Sun above the plane of 18 pc (Arendt *et al.* 1998), while Cohen (1995) gives 15.5 pc and Humphreys & Larsen (1995) give 20.5 pc. Note that the spatial components and the volume element $s^2 ds$ do not depend on the star type i and can be precomputed for a given line of sight before doing the loop over star types. This greatly speeds up the calculation of the model. The upper limit S is set at a radius of 15 kpc from the Galactic center. The local density

ρ_\circ , the vertical scale height h_z , the absolute magnitudes M_λ and their standard deviation σ_i , and the weights f_D, f_A, f_R, f_B and f_H all depend on the star type indexed by i . These parameters are taken from Table 2 in WCVWS, except for the absolute magnitudes at 3.5 & 4.9 μm , for which we use the extrapolated values from Arendt *et al.* (1998).

By directly computing the differential counts, we have no need of the 5 point approximation to the Gaussian used by WCVWS for the absolute magnitude distribution. The exact Gaussian gives larger source counts than the 5 point approximation by an amount $\mathcal{O}(10^{-1}\sigma^2)$ which amounts to about 10% for the lower main sequence stars that dominate the faint high latitude counts.

The disk is assumed to be an exponential disk,

$$D(\vec{r}) = \exp[(R_\circ - R)/h_R] \quad (4)$$

where $R = \sqrt{x^2 + y^2}$ is the radius in cylindrical coordinates. The z dependence has been factored out since it varies with star type. The radial scale is $h_R = 3.5$ kpc and the solar position is at $R_\circ = 8.5$ kpc.

The spiral arms have the same exponential radial dependence as the disk, so this has been factored out. The spiral arm function has only two values corresponding to being in or out of an arm. Define θ such that $x = -R \cos \theta$ and $y = -R \sin \theta$. Thus $\theta = 0$ at the solar position. The arms are defined as logarithmic spirals, based on the H II observations of Georgelin & Georgelin (1976), starting at R_{min} and θ_{min} and extending over an angular extent of E_i but having a fixed radial width of W_i . Then the arm function is given by

$$A(\vec{r}) = C_{arms} \prod_{j=1}^6 T(|R_{min_i} \exp[(\theta - \theta_{min_i})/\alpha_i] - R| < W_i/2) T(\theta - \theta_{min_i} < E_i) \quad (5)$$

where $\theta - \theta_{min}$ is taken modulo 2π and the truth function $T()$ is 1 if its argument is true, and 0 for false arguments. The arm normalization is given by $C_{arms} = 5$. The parameters for the six arms are given in Table 1. Figure 1 shows the pattern of the spiral arms and the molecular ring in the model. Note that the Sun is just barely within the sixth arm.

The halo function, taken from the Young (1976) approximation to the deprojected de Vaucouleurs $r^{1/4}$ intensity law, is given by

$$H(\vec{r}) = C_{halo} \frac{\exp(-b\xi)}{\xi^{7/2} \sqrt{32b}} \quad (6)$$

with $b = 7.66924944$, and

$$\xi = \left[\left(\frac{x}{x_H} \right)^2 + \left(\frac{y}{y_H} \right)^2 + \left(\frac{z}{z_H} \right)^2 \right]^{1/8} \quad (7)$$

with $x_H = y_H = 2.83$ kpc, and $z_H = 2.264$ kpc. The normalization is set so $H = 0.002$ at the solar position.

The molecular ring density enhancement is radially Gaussian with the same stellar type dependent vertical scale height as the disk, so

$$R(\vec{r}) = C_{ring} \exp(-0.5(R - R_{ring})^2 / \sigma_{ring}^2) \quad (8)$$

The radial position of the ring is at $R_{ring} = 0.45R_\odot$ and the radial width is given by $\sigma_{ring} = 0.064R_\odot$, and the ring normalization is $C_{ring} = 25$.

The bulge function, proposed by Bahcall (1986) and chosen by Cohen (1994), is given by

$$B(\vec{r}) = C_{bulge} \frac{\exp(-\chi^3)}{\chi^{1.8}} \quad (9)$$

with

$$\chi = \left[\left(\frac{x}{x_B} \right)^2 + \left(\frac{y}{y_B} \right)^2 + \left(\frac{z}{z_B} \right)^2 \right]^{1/2} \quad (10)$$

with bulge scales $x_B = y_B = 2$ kpc, $z_B = 1.25$ kpc, and normalization $C_{bulge} = 3.6$.

Since extinction from dust affects IR wavelengths much less than shorter wavelengths, this model employs a smooth exponential extinction law. The assumed absorption is given by:

$$\frac{dA_\lambda}{ds} = A_{\lambda_\odot} \exp \left(-\frac{R - R_\odot}{h_{R\ dust}} - \frac{|z|}{h_{z\ dust}} \right), \quad (11)$$

where A_{λ_\odot} is the passband dependent absorption per unit length in the solar vicinity, s is the distance along the line of sight to the current position, and $h_{R\ dust} = 3.5$ kpc and $h_{z\ dust} = 0.1$ kpc are the respective radial and z-component scale lengths for the dust. The solar neighborhood dust absorption was assumed to be 0.07 mag kpc $^{-1}$ at K (WCVWS). This results in $A_{V_\odot} = 0.62$ mag kpc $^{-1}$ using the interstellar extinction law determined by Rieke & Lebofsky (1985). This value was simply scaled appropriately for other wavelengths. The extinction calculation adopted the midpoint of the line of sight increment as the location of the stellar types.

3.2. Comparison with Observation

K predictions of the model have been compared with: the north galactic pole counts of Elias (1978); six high galactic latitude fields of the 2MASS survey; and, for completeness, the galactic plane observations of Eaton, Adams & Giles (1984, hereafter EAG). Both Elias (1978) and EAG provide cumulative counts while we have computed differential counts from the 2MASS catalog.

Figure 2 shows the comparison of observed cumulative star counts with model predictions at the NGP. The model shows excellent agreement with the Elias (1978) observations. The model star counts for each galactic component have also been plotted and show the dominance of the disk which holds for galactic latitudes $|b| \geq 20^\circ$. Table 2 gives the over or under counting percentages versus magnitude. The model predictions are within about 20% of the observed counts.

The partial release of 2MASS data allows us to compare the starcount model to reality in several high latitude fields. Figure 3 shows the comparison between observed differential counts and model star counts for these regions. The model accurately predicts the counts in these regions with the exception of the low magnitude stars which saturate the 2MASS detectors. This saturation may explain the paucity of bright stars compared to the model. Table 3 gives the percentage over or under count in the 2MASS fields versus magnitude. The actual counts are on average¹ 0.89 ± 0.05 times the model counts for the range $6 < K < 12$ in the 4 fields with $|b| > 45^\circ$. This $\sim 10\%$ overprediction in the $6 < K < 12$ range is consistent with the 11% overprediction of integrated counts found by Gorjian *et al.* (2000) in the $(l, b) = (337^\circ, 76^\circ)$ field for the range $9 < K < 12$.

One observes an extremely tight correlation between the model and EAG’s observations in the galactic plane for all but directly towards the galactic center and towards $l = 30^\circ$, where the model respectively over counts brighter stars and under counts overall. This comparison is shown in Figure 4 and Table 4. Hammersley *et al.* (1999) find the Cohen model under predicts the bright star contribution near the galactic center when compared with the Two Micron Galactic plane Survey (TMGS). The high density of stars in the galactic center makes confusion a serious problem. Since at $l = 30^\circ$ one looks tangential to the molecular ring, the under prediction there probably stems from an incomplete treatment of the ring component. More observational insight into the mixture of stellar types and density of the ring would aid in modeling this galactic component. Since we are concerned only with high latitude regions, we do not pursue either issue further.

We are interested in high galactic latitudes where the contamination to the CIRB from stars and the ISM is minimal. Figure 5 synthesizes the model performance for high galactic latitude regions over a wide range of magnitudes. We constructed differential counts from the Elias (1978) results and computed an average over the six fields of the 2MASS survey. The model is consistent with the data in these high latitude regions of interest. The model is in particularly good agreement with the recent 2MASS results.

4. Calculating the CIRB

4.1. Model histograms

The predicted histograms were calculated using a Monte Carlo method based on $N(< m)$ curves calculated from the WCVWS model. Here $N(< m)$ is the number of stars per unit solid angle brighter than magnitude m . In order to simulate the DIRBE maps, the flux from a star has to be divided up among several pixels in the same way that the actual DIRBE divided up the flux. Flux always extends beyond the 5 pixel blanking area used for bright source removal by Arendt *et al.* (1998), and often extends beyond the 9 pixel blanking area used by Kashlinsky,

¹A weighted median was used with uncertainties given by $\max(N^{-1/2}, 0.1)$.

Mather & Odenwald (1996). In this work we have divided the flux into 16 pixels with weights w_i for $i = 1 \dots 16$. The flux division will depend on where within a pixel a star is located, and will also depend on where the pixel is relative to the cube used to define the quadrilateralized spherical cube pixel scheme used by COBE. We have sampled the actual flux division for DIRBE by locating the brightest 8 stars within the region with $\sin|b| > 0.9$. Thus we obtain 8 different sets of weights, w_{ij} , for $i = 1 \dots 16$ and $j = 1 \dots 8$, which are shown in Table 5. Note that $\sum_i w_{ij} = 1$ for all j . We divide each DIRBE pixel into 8 subpixels, and use the weights w_{ij} if the star falls into the j^{th} subpixel.

For each sub-pixel one calculates n drawn from a Poisson distribution with mean $\mu = 1$. Then one finds n magnitudes m chosen so that $\Omega_{sp}N(< m) = U$ where U is a random number drawn from a distribution uniform between 0 and 1, and Ω_{sp} is the solid angle of a sub-pixel. This can be done quite quickly by making a spline fit to $N(< m)$ using N as the independent variable. The flux of these stars are given by $F = F_0 10^{-0.4m}$, where F_0 is the flux for a 0^{th} magnitude star. The faintest star produced by this method has magnitude m_1 such that $\Omega_{sp}N(< m_1) = 1$. Typical values of m_1 are ≈ 11.7 . A Gaussian random number representing stars fainter than m_1 is chosen with a mean

$$F_{faint} = F_0 \Omega_{sp} \int_{m_1}^{\infty} 10^{-0.4m} [dN(< m)/dm] dm \quad (12)$$

and a variance

$$\sigma_{faint}^2 = F_0^2 \Omega_{sp} \int_{m_1}^{\infty} 10^{-0.8m} [dN(< m)/dm] dm. \quad (13)$$

The flux in each sub-pixel is then weighted by w_{ij} , and the resulting weighted sum of 128 subpixels (8 in each of the 16 neighboring pixels) gives the Monte Carlo intensity value for one pixel. A Gaussian random number with zero mean and standard deviation equal to the detector noise given by Hauser *et al.* (1998) is then added to the intensity to give the final value.

In order to compute a model histogram this process is repeated many times. For the model shown in Figure 6, nearly 4 million independent pixel intensity values were generated. This is 100 times more values than the 39,356 pixels in the region with $\sin|b| > 0.9$ which gives the data histogram shown in the figure. Note that pixel values in the real maps are not independent, because pixels close enough to be in the DIRBE beam at the same time are correlated. Our Monte Carlo method does not model this correlation because the correlation is a 2-point property of the map, and we are only comparing histograms which are 1-point properties of the map.

4.2. Histogram Fitting

To find the CIRB, one simply slides the model histogram along the flux axis until it closely matches the DIRBE data histogram. The amount required to align the histograms, ΔI , yields an estimate of the CIRB. A “by eye” best fit yields $\Delta I \approx 12 \text{ kJy sr}^{-1}$. Figure 6 shows the model histogram along with the DIRBE data histogram on a linear intensity scale to facilitate sliding.

We applied a χ^2 method to percentile values extracted from the histograms to quantify the best fit. We found the intensity values for the 5th, 15th, ... 95th %-tiles in both the model and data histograms. The model fit assumes that the actual data histogram intensity at a given percentile, Y_i , is given by $p_1 + p_2 F_i$, where F_i is the corresponding intensity in the model histogram, p_1 is the cosmic background and p_2 is a flux calibration factor. These percentile values are highly correlated because they are cumulative statistics. But the covariance matrix is easily calculated. Let $I(f)$ be the intensity at the 100^{fth} percentile. The covariance matrix of the percentiles is given by

$$C_{ij} = \frac{f_i(1 - f_j)}{N} \left. \frac{\partial I}{\partial f} \right|_i \left. \frac{\partial I}{\partial f} \right|_j. \quad (14)$$

Given these correlated data points, we minimize χ^2 as follows. Let $V_{ij} = \partial Y_i / \partial p_j$ be a matrix of partial derivatives of the data with respect to the parameters. Note that $V_{i1} = 1$ and $V_{i2} = F_i$. Then the parameters are found using

$$P = [V^T C^{-1} V]^{-1} V^T C^{-1} Y. \quad (15)$$

The covariance matrix of the fitted parameters is $[V^T C^{-1} V]^{-1}$. Because the pixel values in the actual histograms are not independent, we have scaled the standard deviations of the parameters by $\sqrt{\chi_{min}^2 / \nu}$ where $\nu = 8$ is the number of degrees of freedom in the fit. Figure 7 shows the best fit lines for both the two parameter case and the one parameter fit with p_2 forced to be unity. Once the parameters are found, the model histogram can be scaled and plotted over the data as shown in Figure 8, which also shows where the percentiles fall within the distribution.

We have chosen this form of fitting instead of the Kolmogorov-Smirnov test because the K-S test requires a fixed predefined comparison distribution, while in our case the model distribution has parameters p_1 and p_2 which are derived from the data.

4.3. Tests of the method

The effect of various perturbations to the modeling on the derived parameters were tested by simulation. Three test point spread functions were tried as replacements for the observed DIRBE beam. These were a 4 pixel top hat, and 5 pixel top hat, and beam giving w_i equal to a Gaussian function of i which corresponds to a shape on the sky of $\exp(-\beta\theta^4)$. The w_i 's for these assumption are listed at the bottom of Table 5. The hard-edged top hat beams lead to a larger value of the CIRB by about 0.9 kJy sr⁻¹ at 3.5 μ m. The $\exp(-\beta\theta^4)$ beam gave the same CIRB as the observed DIRBE beam to within 0.1 kJy sr⁻¹. We have also run eight tests using just one of the star profiles at a time. The standard deviation of the mean of these tests is 0.11 kJy sr⁻¹ at 2.2 μ m and 0.06 kJy sr⁻¹ at 3.5 μ m.

Even though our method is independent of the relative calibration between DIRBE fluxes and magnitudes, a comparison with previous work requires knowledge of F_0 . While most of the stars in

Table 5 are variable, we can still find their median $3.5 \mu\text{m}$ magnitudes in Gezari, Schmitz & Mead (1987) and compute values for $F_0(L)$ at $3.5 \mu\text{m}$ which are given in Table 6. The median of these $F_0(L)$'s is 254 Jy and the mean is 265 ± 12 Jy which agree with the $F_0(L) = 263$ Jy in Gorjian *et al.* (2000).

Tests that excluded the detector noise ($\sigma = 1.05 \text{ kJy sr}^{-1}$ per pixel at $3.5 \mu\text{m}$) given by Hauser *et al.* (1998) changed the derived CIRB by $-0.20 \text{ kJy sr}^{-1}$ at $2.2 \mu\text{m}$ and $-0.30 \text{ kJy sr}^{-1}$ at $3.5 \mu\text{m}$. The noise quoted by Hauser *et al.* (1998) may contain some confusion noise due to unresolved stars which are already included in our Monte Carlo histograms and should not be counted twice.

The histogram fitting method is independent of the adopted DIRBE flux at 0^{th} magnitude because the free parameter p_2 multiplies the model fluxes. Since the star counts in the region of interest are nearly a power law, this also makes the derived CIRB values nearly independent of a constant scaling factor applied to the counts, since for a power law, scaling the counts is equivalent to a scaling of the fluxes. We have adopted a count scaling factor of 0.9 based on comparison of the model to the high latitude 2MASS fields, and varying this factor by ± 0.1 only changes the derived CIRB by $\mp 0.52 \text{ kJy sr}^{-1}$ at $2.2 \mu\text{m}$ and $\mp 0.43 \text{ kJy sr}^{-1}$ at $3.5 \mu\text{m}$.

Any change in the differential source counts, dN/dm , from the starcount model will have some effect on the derived CIRB, and different changes to the model that produce the same change in dN/dm will produce the same change in the CIRB. Table 7 shows how the derived CIRB changes when the differential star counts are increased by a ‘‘bump’’ that is 25% high, centered at m_b and 1 magnitude wide (FWHM):

$$\left(\frac{dN}{dM}\right)' = \exp(0.25 \max(0, 1 - |m - m_b|)) \frac{dN}{dM}. \quad (16)$$

Increasing the bright star count causes the derived CIRB to go up, while increasing the faint star count causes the derived CIRB to go down. The corresponding changes in the derived CIRB using the Arendt *et al.* (1998) method, shown in the last two columns of Table 7, are generally larger and always cause the CIRB to go down.

The model has an outer radius of 15 kpc. Changing this cutoff to 25 kpc reduces the derived CIRB by only $-0.08 \text{ kJy sr}^{-1}$ at $2.2 \mu\text{m}$ and $-0.13 \text{ kJy sr}^{-1}$ at $3.5 \mu\text{m}$. If we triple the halo density of all lower main sequence stars (later than G2V) this changes the derived CIRB by only $-0.58 \text{ kJy sr}^{-1}$ at $2.2 \mu\text{m}$ and $-0.20 \text{ kJy sr}^{-1}$ at $3.5 \mu\text{m}$ in the HQB region. These results are not surprising since the halo makes such a small contribution to the star counts in Figure 2.

We also used several regions to test for isotropy: the NGP with $\sin(b) > 0.96$, the SGP with $\sin(b) < -0.96$, the NEP with $\sin \beta > 0.96$, a region with $|\sin |b| - \sqrt{1/2}| < 0.035$ and $|\beta| > 45^\circ$ (B45), and the High Quality B (HQB) region from Hauser *et al.* (1998) with $|b| > 60^\circ$ and $|\beta| > 45^\circ$. The CIRB's derived from these regions, shown in Table 8, are very consistent with each other and with the values derived by Gorjian *et al.* (2000) by direct measurement and subtraction of stars in the ‘‘dark spot’’ in the $2.2 \mu\text{m}$ band, and reasonably consistent at $3.5 \mu\text{m}$. If we fit the values in Table 8 to $A + G \csc |b|$ or $A + Z \csc |\beta|$, we find no trend with either b or β at $2.2 \mu\text{m}$, but a slope

of $Z = 2.65 \text{ kJy sr}^{-1}$ per unit of $\csc |\beta|$ at $3.5 \mu\text{m}$. This indicates a problem with our zodiacal light model but the slope is smaller than our zodiacal model error estimate of 3.3 kJy sr^{-1} .

Finally, in regions with a gradient in the star density, such as the NEP region, it is important to allow for this gradient. Making an average starcount by running the starcount model for several subregions, and then generating one histogram for the whole region from the average starcounts, will give an incorrect result for the CIRB. The histogram making operation and the averaging operation do not commute, and the pixel values that go into the actual data histogram are generated from the stars within a single instrument field of view. The correct procedure is to calculate the starcount model for many small subregions, generate individual histograms for these subregions, and then average the histograms together. We have used between 4 and 8 subregions in our fields.

The position of the Sun near the edge of a spiral arm leads to a discontinuity across the sky on a line through the galactic poles from longitude $l = \tan^{-1}(4.57) = 78^\circ$ to $l = 258^\circ$. The amplitude of this discontinuity is 9% in dN/dm at $L = 7$ and 4.6% in the total integrated intensity at $3.5 \mu\text{m}$. Analyzing the NGP data using all subregions, both inside and outside the discontinuity, gives a CIRB of 16.65 and $14.27 \text{ kJy sr}^{-1}$ at 2.2 and $3.5 \mu\text{m}$, as reported in Table 8. Using model histograms computed only from star counts inside the discontinuity gives a CIRB of 16.16 and $14.07 \text{ kJy sr}^{-1}$, while using only star counts from outside the discontinuity gives 16.39 and $14.51 \text{ kJy sr}^{-1}$. Thus while the model is not perfect, the histogram method is quite insensitive to its faults.

5. Discussion

At this point we have independent estimates for the CIRB at 2.2 and $3.5 \mu\text{m}$. These estimates from the histogram fitting method are consistent with the independent estimates of the CIRB obtained by direct subtraction of measured stars in Gorjian *et al.* (2000). Now we can combine the 2.2 and $3.5 \mu\text{m}$ maps following the technique of Dwek & Arendt (1998), which gives a CIRB estimate at $3.5 \mu\text{m}$ if the $2.2 \mu\text{m}$ CIRB is known.

We proceed by fitting the $3.5 \mu\text{m}$ map to a linear combination of the $2.2 \mu\text{m}$ map, the $100 \mu\text{m}$ map, a constant and $\csc \beta$. A fit that minimizes the sum of absolute values of the errors in the region $\sin |b| > 0.4$ and $\sin |\beta| > 0.4$ gives

$$I_{3.5} = 2.68 + 2.66 \csc |\beta| + 0.4976 I_{2.2} + 0.00094 I_{100} \text{ kJy sr}^{-1}. \quad (17)$$

This fit gives the same slope *vs.* $\csc |\beta|$ as the fit to the data in Table 8. The coefficient of the $2.2 \mu\text{m}$ map becomes 0.3128 when the fit is expressed in $\text{nW m}^{-2} \text{ sr}^{-1}$ instead of kJy sr^{-1} , in excellent agreement with the fit found by Dwek & Arendt (1998). The coefficient of the $100 \mu\text{m}$ map is only one-half of the value found by Arendt *et al.* (1998) in regions close to the galactic plane. The constant term of 2.68 kJy sr^{-1} is not the CIRB, but rather the displacement of the $3.5 \mu\text{m vs. } 2.2 \mu\text{m}$ correlation from the origin (see eq. [18] for the CIRB). Repeating the fit in equation 17 using the DIRBE ZSMA maps produced using the Kelsall *et al.* (1998) model gives $3.57 \csc |\beta|$ for the

dependence on ecliptic latitude, so our new zodiacal light model gives a smaller residual slope than the Kelsall *et al.* (1998) model. Note that while a non-zero slope *vs.* $\csc|\beta|$ clearly indicates a problem with the zodiacal model, a small slope does not necessarily mean a small zero-point error.

We can construct a map of the $3.5\ \mu\text{m}$ residual after subtracting the galactic contributions due to stars and the ISM using

$$\begin{aligned} R_{3.5} &= I_{3.5} - 0.4976(I_{2.2} - I_{\circ}(2.2)) - 0.00094(I_{100} - I_{\circ}(100)) \\ &= I_{3.5} - 0.4976I_{2.2} - 0.00094I_{100} + 8.8\ \text{kJy sr}^{-1} \end{aligned} \quad (18)$$

where $I_{\circ}(2.2) = 16.9\ \text{kJy sr}^{-1}$ and $I_{\circ}(100) = 0.4\ \text{MJy sr}^{-1}$. Figure 9 shows a map of this residual which is nearly isotropic over the high galactic latitude sky. Figure 10 compares the histogram of the original zodi-subtracted $3.5\ \mu\text{m}$ map in the region with $b > 45^{\circ}$ and $\beta > 45^{\circ}$ to the histogram of the residual map in same region. The histogram of the residual, shown in Figure 10, is very sharply peaked. A Gaussian fit to the highest three bins gives $14.23 \pm 1.57\ \text{kJy sr}^{-1}$ for the mean residual and its single pixel standard deviation. Both the map and the histogram show that the CIRB estimate obtained by combining the 2.2 and $3.5\ \mu\text{m}$ maps is quite isotropic.

Based on our tests, we have set up the error budget shown in Table 9. The largest term is the zodiacal light error which is estimated at 5% of the zodiacal intensity at the ecliptic poles. The next largest term is an estimate for errors from the starcount model other than constant count scaling or flux scaling factors, for which we have used the quadrature sum of the values in Table 7, which were based on 25% errors in the starcounts. The ISM error is taken as 50% of the ISM correction in the HQB region. The DIRBE noise error is taken as 50% of the difference between the no noise and with noise CIRB’s. The DIRBE beam error is based on the scatter among the eight different stars in Table 5 when used one at a time. The standard deviation of the mean of the five histogram fitting results in Table 8 is included as “scatter”. The quadrature sum of the errors is used as our final uncertainty estimate.

Given that three independent methods show the existence of a CIRB at 2.2 and $3.5\ \mu\text{m}$, it is worth investigating why Hauser *et al.* (1998) did not find it. One reason is that the mean of the unblanked pixels, which was used by Arendt *et al.* (1998), is a very inefficient statistical estimator when the noise is dominated by confusion. Consider N samples $x_i = C + y_i$, where y_i are independent identically distributed random variables with known probability density function $p(y)$. Here the x_i are pixel data values, C is the CIRB, and $p(y)$ is the normalized model histogram. Then the likelihood L is given by

$$\begin{aligned} \ln[L(\hat{C})] &= \sum_{i=1}^N \ln[p(x_i - \hat{C})] \\ &\approx N \int \ln[p(x - \hat{C})]p(x - C)dx \\ &\approx \ln[L_{max}] - \frac{N}{2\sigma_1^2}(\hat{C} - C)^2 + \dots \end{aligned} \quad (19)$$

Using the model histogram in Figure 6, we find that standard deviation of the CIRB for a sample size of 1 pixel is $\sigma_1 = 6.5 \text{ kJy sr}^{-1}$. But the corresponding standard deviation for the mean of the unblanked pixels is given by $\sigma_{faint} = 50.3 \text{ kJy sr}^{-1}$ from equation (13) with the one pixel Ω and m_1 set to the blanking level of $L = 3$. Thus the histogram fitting method would reach a statistical noise level of 1 kJy sr^{-1} for $N = 43$ pixels while the mean of unblanked pixels needs 2,526 pixels to reach the same noise level.

However, since DIRBE observed $> 10^5$ high latitude pixels, statistical efficiency is not a major concern, but systematic error sensitivity is. The faint source model (FSM) of Arendt *et al.* (1998) is the same as the model we have used to predict model histograms, but Arendt *et al.* (1998) were much more sensitive to model parameters than this paper. The FSM in Arendt *et al.* (1998) contributed 67 kJy sr^{-1} per unit of $\csc |b|$ at $2.2 \mu\text{m}$ and 40 kJy sr^{-1} at $3.5 \mu\text{m}$. Thus the sensitivity of the CIRB to $\pm 10\%$ model over or under predictions at $2.2 \mu\text{m}$ is about $\mp 6.7 \text{ kJy sr}^{-1}$ which is 12.8 times higher than the sensitivity of our histogram method. At $3.5 \mu\text{m}$ the Arendt *et al.* (1998) method is 9.2 times more sensitive to model over or under predictions than our histogram method. And the histogram method is completely insensitive to changes in the flux at 0^{th} magnitude while the Arendt *et al.* (1998) method is directly proportional to errors in F_0 . The combined effects of a 10% overprediction by the model, and an 8% change in F_0 at $3.5 \mu\text{m}$ (Gorjian *et al.* 2000), explain most of the galactic slope in the residual maps of Arendt *et al.* (1998) which was -27% of the FSM slope. At $2.2 \mu\text{m}$, Gorjian *et al.* (2000) found the Arendt *et al.* (1998) F_0 was correct, so one would expect the galactic slope in the residual maps of Arendt *et al.* (1998) to be reduced to -19%, while it was actually -18% of the FSM.

6. Conclusion

Using the unweighted mean of the 5 histogram fitting results in Table 8, we obtain an estimate of the CIRB of $16.9 \pm 4.4 \text{ kJy sr}^{-1}$ at $2.2 \mu\text{m}$ and $14.4 \pm 3.7 \text{ kJy sr}^{-1}$ at $3.5 \mu\text{m}$, where the errors are dominated by zodiacal light model uncertainties. These values compare quite well with the values obtained by Gorjian *et al.* (2000) using direct subtraction of measured stars in the dark spot. Thus we have obtained CIRB values at 2.2 and $3.5 \mu\text{m}$ that are consistent with the dark spot values, even though the sky areas used are disjoint and the techniques used are very different. Our values are also consistent with the Hauser *et al.* (1998) upper limits, and with the Dwek & Arendt (1998) correlation between the 2.2 and $3.5 \mu\text{m}$ CIRB values, as shown in Table 10. The dominant uncertainty is in the zodiacal light model, which gives a systematic error common to both the dark spot and the histogram values for the CIRB.

Our values show that the near IR background has a bolometric intensity that is similar to the bolometric intensity of the far IR background found by Hauser *et al.* (1998). Thus roughly 50% of the radiation produced by galaxies is absorbed by dust and re-radiated in the far IR.

EDR acknowledges support from NASA GSRP Fellowship NGT5-50173. The *COBE* datasets were developed by the NASA Goddard Space Flight Center under the guidance of the COBE Science Working Group and were provided by the NSSDC. This publication makes use of data products from the Two Micron All Sky Survey, which is a joint project of the University of Massachusetts and the Infrared Processing and Analysis Center, funded by the National Aeronautics and Space Administration and the National Science Foundation. We thank Rick Arendt for making many useful comments and criticisms of a draft of this paper.

REFERENCES

- Arendt, R., Odegard, N., Weiland, J., Sodroski, T., Hauser, M., Dwek, E., Kelsall, T., Moseley, S. H. Jr., Silverberg, R., Leisawitz, D., Mitchell, K., Reach, W. & Wright, E. 1998, ApJ, 508, 74-105
- Bahcall, J.N. 1986, ARA&A, 24, 577
- Carr, B.J. 1992, in “The Infrared and Submillimetre Sky after COBE”, Proceedings of the NATO Advanced Study, ed. M. Signore & C. Dupraz (Dordrecht, Kluwer), p. 213
- Cohen, M. 1994, AJ, 107, 582
- Cohen, M. 1995, ApJ, 444, 874
- Dwek, E. & Arendt, R. 1998, ApJ, 508, L9 (DA98)
- Eaton, N., Adams, D.J. & Giles A.B. 1984, MNRAS, 208, 241 (EAG)
- Elias, J.H. 1978, AJ, 83, 791
- Fukugita, M. & Kawasaki, M. 1993, ApJ, 402, 58
- Funk, B., Magnussen, N., Meyer, H., Rhode, W., Westerhoff, S. & Wiebel-Sooth, B. 1998, Astroparticle Physics, 9, 97-103.
- Gardner, J. P., Cowie, L. L. & Wainscoat, R. J. 1993, ApJ, 415, L9-L12.
- Georgelin, Y.M. & Georgelin, Y.P. 1976, A&A, 49, 57
- Gezari, D., Schmitz, M. & Mead, J. 1987, NASA Reference Publication 1196.
- Gorjian, V., Wright, E. & Chary, R. 2000, ApJ, submitted. astro-ph/9909428
- Hammersley, P. L., Cohen, M., Garzón, F., Mahoney, T., & López-Corredoira, M. 1999, MNRAS, 308, 333

- Hauser, M.G., Kelsall, T., Moseley, Jr., S.H., Silverberg, R.F., Murdock, T., Toller, G., Spiesman, W., & Weiland, J. 1991, in “After the First Three Minutes”, AIP Conference Proceedings 222, ed. S.S. Holt, C.L. Bennett, & V. Trimble (New York, AIP), p. 161
- Hauser, M. G., Arendt, R. G., Kelsall, T., Dwek, E., Odegard, N., Weiland, J. L., Freudenreich, H. T., Reach, W. T., Silverberg, R. F., Moseley, S. H., Pei, Y. C., Lubin, P., Mather, J. C., Shafer, R. A., Smoot, G. F., Weiss, R., Wilkinson, D. T. & Wright, E. L. 1998, ApJ, 508, 25
- Humphreys, R. M. & Larsen, J. A. 1995, AJ, 110, 2183
- Kashlinsky, A., Mather, J. & Odenwald, S. 1996, ApJ, 473, 681-705.
- Kelsall, T., Weiland, J. L., Franz, B. A., Reach, W. T., Arendt, R. G., Dwek, E., Freudenreich, H. T., Hauser, M. G., Moseley, S. H., Odegard, N. P., Silverberg, R. F. & Wright, E. L. 1998, ApJ, 508, 44
- Matsumoto, T., Akiba, M., & Murakami, H. 1988, ApJ, 332, 575
- Matsuura, S., Kawada, M., Matsuhara, H., Matsumoto, T., Noda, M., & Tanaka, M. 1994 PASP, 106, 770
- Partridge, B. & Peebles, P. J. E. 1967, ApJ, 148, 377
- Rieke, G.H., & Lebofsky, M.J. 1985, ApJ, 288, 618
- Wainscoat, R.J., Cohen, M., Volk, K., Walker, H.J., & Schwartz, D.E. 1992, ApJS, 83, 111 (WCVWS)
- Wright, E. 1997, BAAS, 29, 1354.
- Wright, E. 1998, ApJ, 496, 1-8.
- Young, P.J. 1976, AJ, 81, 807

Table 1. Spiral Arm Representation

Arm/Spur index	α	R_{min} (kpc)	θ_{min} (rad)	E (rad)	W (kpc)
1	4.25	3.48	0.000	6.00	0.75
2	4.25	3.48	3.141	6.00	0.75
3	4.89	4.90	2.525	6.00	0.75
4	4.89	4.90	5.666	6.00	0.75
5	4.57	8.10	5.847	0.55	0.30
6	4.57	7.59	5.847	0.55	0.30

Table 2. $100 \times \ln(\text{ACTUAL}/\text{MODEL})$ for the NGP region (Elias)

mag	$b = 90$
1.00	-18 ± 39
2.00	-54 ± 30
3.00	-11 ± 21
3.50	-22 ± 17
6.50	34 ± 42
7.50	-10 ± 33
8.50	5 ± 24

Table 3. $100 \times \ln(\text{ACTUAL}/\text{MODEL})$ counts in regions from the 2MASS catalog.

mag	$l = 34$ $b = 82$ $\Omega = 7.9(^{\circ})^2$	$l = 286$ $b = 77$ $\Omega = \pi(^{\circ})^2$	$l = 341$ $b = 75$ $\Omega = 29.5(^{\circ})^2$	$l = 225$ $b = 54$ $\Omega = \pi(^{\circ})^2$	$l = 205$ $b = 19$ $\Omega = \pi(^{\circ})^2$	$l = 158$ $b = -41$ $\Omega = 3.9(^{\circ})^2$
3.5
4.5	-100 ± 58	27 ± 71
5.5	-89 ± 71	...	-54 ± 31	-76 ± 99	61 ± 34	51 ± 41
6.5	-4 ± 32	-3 ± 50	-24 ± 18	-43 ± 58	3 ± 29	-49 ± 45
7.5	-51 ± 29	-46 ± 45	-29 ± 14	-41 ± 41	-12 ± 21	-5 ± 25
8.5	-2 ± 17	-4 ± 27	4 ± 09	-41 ± 31	-49 ± 17	0 ± 18
9.5	8 ± 12	-33 ± 22	5 ± 06	-21 ± 20	-9 ± 10	13 ± 13
10.5	1 ± 08	10 ± 12	-13 ± 05	-11 ± 13	12 ± 07	-8 ± 10
11.5	-13 ± 06	-13 ± 09	-16 ± 03	-10 ± 08	8 ± 05	6 ± 06
12.5	-22 ± 04	-19 ± 07	-19 ± 02	-12 ± 06	10 ± 04	-11 ± 05
13.5	-8 ± 03	-8 ± 05	-6 ± 02	2 ± 04	6 ± 03	-22 ± 04
14.5	30 ± 02	26 ± 04	32 ± 01	21 ± 03	9 ± 02	15 ± 03
15.5	19 ± 02	62 ± 03	36 ± 01	36 ± 03	-24 ± 02	-47 ± 03

Table 4. $100 \times \ln(\text{ACTUAL}/\text{MODEL})$ for the EAG regions

mag	$l = 0$ $\Omega = 144(^{\circ})^2$	$l = 10$ $\Omega = 99(^{\circ})^2$	$l = 20$ $\Omega = 103(^{\circ})^2$	$l = 30$ $\Omega = 384(^{\circ})^2$	$l = 40$ $\Omega = 104(^{\circ})^2$	$l = 50$ $\Omega = 121(^{\circ})^2$	$l = 60$ $\Omega = 101(^{\circ})^2$
5.00	-7 ± 58
5.50	49 ± 33
6.00	58 ± 24
6.50	43 ± 20
7.00	-216 ± 58	-29 ± 45	-26 ± 41	43 ± 16	-83 ± 71	-43 ± 58	-5 ± 58
7.50	-244 ± 41	-2 ± 30	10 ± 27	33 ± 13	-21 ± 41	-40 ± 45	-2 ± 45
8.00	-178 ± 21	-17 ± 26	5 ± 22	36 ± 11	-7 ± 30	-37 ± 35	1 ± 35
8.50	-110 ± 11	-18 ± 20	18 ± 17	32 ± 9	13 ± 22	-5 ± 24	6 ± 28
9.00	-24 ± 7	4 ± 15	18 ± 14	26 ± 7	-5 ± 19	0 ± 19	-1 ± 23
9.50	9 ± 5	12 ± 12	19 ± 11	23 ± 7	-11 ± 16	1 ± 15	-2 ± 19
10.00	-19 ± 5	-3 ± 11	26 ± 10	9 ± 6	-15 ± 13	-3 ± 13	-20 ± 16
10.50	...	-28 ± 10	25 ± 9	7 ± 5	-8 ± 11	5 ± 10	-7 ± 13
11.00	11 ± 9	6 ± 8	9 ± 10
11.50	5 ± 8	7 ± 7	3 ± 8

Table 5. DIRBE Beam. 10^4 times the flux fraction in pixels from 1 at the peak to the 16th nearest pixel

Source	1	2	3	4	5	6	7	8	9	10	11	12	13	14	15	16
α Boo	2495	1724	1641	1209	1286	683	635	105	181	8	13	7	3	3	4	2
RX Boo	2389	2251	917	1460	392	98	1641	67	164	327	4	55	217	5	4	7
R Aqr	2314	2134	750	1373	1141	81	1052	709	197	118	45	13	8	25	27	12
RT Vir	2278	1839	669	670	2125	459	184	1521	9	38	8	11	166	7	11	7
δ Vir	2274	322	2149	2258	302	184	241	13	2000	20	119	68	11	11	16	13
Y CVn	2207	645	2088	1650	52	1788	8	240	8	8	646	625	9	9	9	7
BK Vir	2244	264	2243	591	1769	1804	18	96	519	14	227	15	49	105	22	21
T Cet	2206	1968	861	1999	321	10	1618	154	619	68	15	72	31	16	29	14
Top Hat 4	2500	2500	2500	2500	0	0	0	0	0	0	0	0	0	0	0	0
Top Hat 5	2000	2000	2000	2000	2000	0	0	0	0	0	0	0	0	0	0	0
$e^{-\beta\theta^4}$	2253	2033	1713	1348	990	680	435	261	145	76	37	17	7	3	1	0

Table 6. DIRBE Calibration at 3.5 μm .

Source	# ^a	median L	DIRBE Flux [Jy]	F_0 in Jy
α Boo	23	-3.12	4500	254.2
RX Boo	10	-2.30	2009	241.5
R Aqr	4	-1.50	1327	334.9
RT Vir	3	-1.40	1073	295.5
δ Vir	6	-1.39	915	254.3
Y CVn	8	-1.51	913	227.2
BK Vir	2	-1.26	805	252.2
T Cet	0	-1.14 ^b	753	262.9

^aThe number of magnitudes for $3.4 \leq \lambda \leq 3.6 \mu\text{m}$ in Gezari *et al.* (1987).

^bInterpolated between the 2.2 and 4.2 μm magnitudes.

Table 7. Effect on the CIRB of increasing the differential star counts by 25% over a 1 mag FWHM bin centered at m_b .

m_b	This paper		Arendt <i>et al.</i> (1998)	
	$\Delta I_{CIRB}(2.2 \mu\text{m})$	$\Delta I_{CIRB}(3.5 \mu\text{m})$	$-\Delta I(K > 4)$	$-\Delta I(L > 3)$
2	0.45 kJy sr ⁻¹	0.07 kJy sr ⁻¹	-0.00 kJy sr ⁻¹	-0.00 kJy sr ⁻¹
3	0.82 kJy sr ⁻¹	0.16 kJy sr ⁻¹	-0.00 kJy sr ⁻¹	-0.66 kJy sr ⁻¹
4	0.90 kJy sr ⁻¹	0.40 kJy sr ⁻¹	-1.13 kJy sr ⁻¹	-1.10 kJy sr ⁻¹
5	0.96 kJy sr ⁻¹	0.38 kJy sr ⁻¹	-2.19 kJy sr ⁻¹	-1.04 kJy sr ⁻¹
6	0.23 kJy sr ⁻¹	-0.08 kJy sr ⁻¹	-1.99 kJy sr ⁻¹	-0.94 kJy sr ⁻¹
7	-0.39 kJy sr ⁻¹	-0.50 kJy sr ⁻¹	-1.66 kJy sr ⁻¹	-0.77 kJy sr ⁻¹
8	-0.65 kJy sr ⁻¹	-0.55 kJy sr ⁻¹	-1.25 kJy sr ⁻¹	-0.58 kJy sr ⁻¹
9	-0.45 kJy sr ⁻¹	-0.23 kJy sr ⁻¹	-0.92 kJy sr ⁻¹	-0.44 kJy sr ⁻¹
10	-0.63 kJy sr ⁻¹	-0.29 kJy sr ⁻¹	-0.76 kJy sr ⁻¹	-0.37 kJy sr ⁻¹
11	-0.44 kJy sr ⁻¹	-0.33 kJy sr ⁻¹	-0.71 kJy sr ⁻¹	-0.34 kJy sr ⁻¹
12	-0.31 kJy sr ⁻¹	-0.40 kJy sr ⁻¹	-0.63 kJy sr ⁻¹	-0.30 kJy sr ⁻¹

Table 8. Comparison of Different Regions: Statistical Errors Only

Region	# of pixels	$\langle \text{csc } b \rangle$	$\langle \text{csc } \beta \rangle$	kJy sr ⁻¹ at	kJy sr ⁻¹ at
				2.2 μm	3.5 μm
Dark Spot	17	1.095	1.289	16.4 ± 2.3	12.8 ± 1.8
NGP	7875	1.021	2.204	16.7 ± 0.4	15.0 ± 0.3
SGP	7875	1.021	2.204	18.9 ± 0.5	17.7 ± 0.3
HQB	8688	1.100	1.296	16.9 ± 0.9	14.2 ± 0.4
B45	8372	1.415	1.151	17.3 ± 0.6	13.4 ± 0.4
NEP	7816	2.204	1.021	14.9 ± 2.0	11.9 ± 1.2

Table 9. CIRB error budget.

Term	Uncertainty	$\Delta I_{CIRB}(2.2\mu\text{m})$	$\Delta I_{CIRB}(3.5\mu\text{m})$
Zodiacal	5%	3.79 kJy sr ⁻¹	3.25 kJy sr ⁻¹
ISM	50%	...	0.85 kJy sr ⁻¹
Starcourt	25%	2.03 kJy sr ⁻¹	1.14 kJy sr ⁻¹
Count scaling	5%	0.26 kJy sr ⁻¹	0.22 kJy sr ⁻¹
Flux scaling	5%
DIRBE noise	50%	0.10 kJy sr ⁻¹	0.15 kJy sr ⁻¹
DIRBE beam	100%	0.11 kJy sr ⁻¹	0.06 kJy sr ⁻¹
scatter	100%	0.64 kJy sr ⁻¹	0.96 kJy sr ⁻¹
Quadrature Sum		4.36 kJy sr ⁻¹	3.69 kJy sr ⁻¹

Table 10. CIRB at 3.5 μm

flux	detector	reference
35.00 kJy sr ⁻¹	theory	Partridge & Peebles (1967)
128.56 kJy sr ⁻¹	rocket	Matsumoto, Akiba, & Murakami (1988)
< 271.83 kJy sr ⁻¹	rocket	Matsuura <i>et al.</i> (1994)
< 26.83 kJy sr ⁻¹	DIRBE	Hauser <i>et al.</i> (1998)
> 11.55 kJy sr ⁻¹	DIRBE	Dwek & Arendt (1998)
12.8 kJy sr ⁻¹	DIRBE	Gorjian <i>et al.</i> (2000)
14.4 kJy sr ⁻¹	DIRBE	this paper

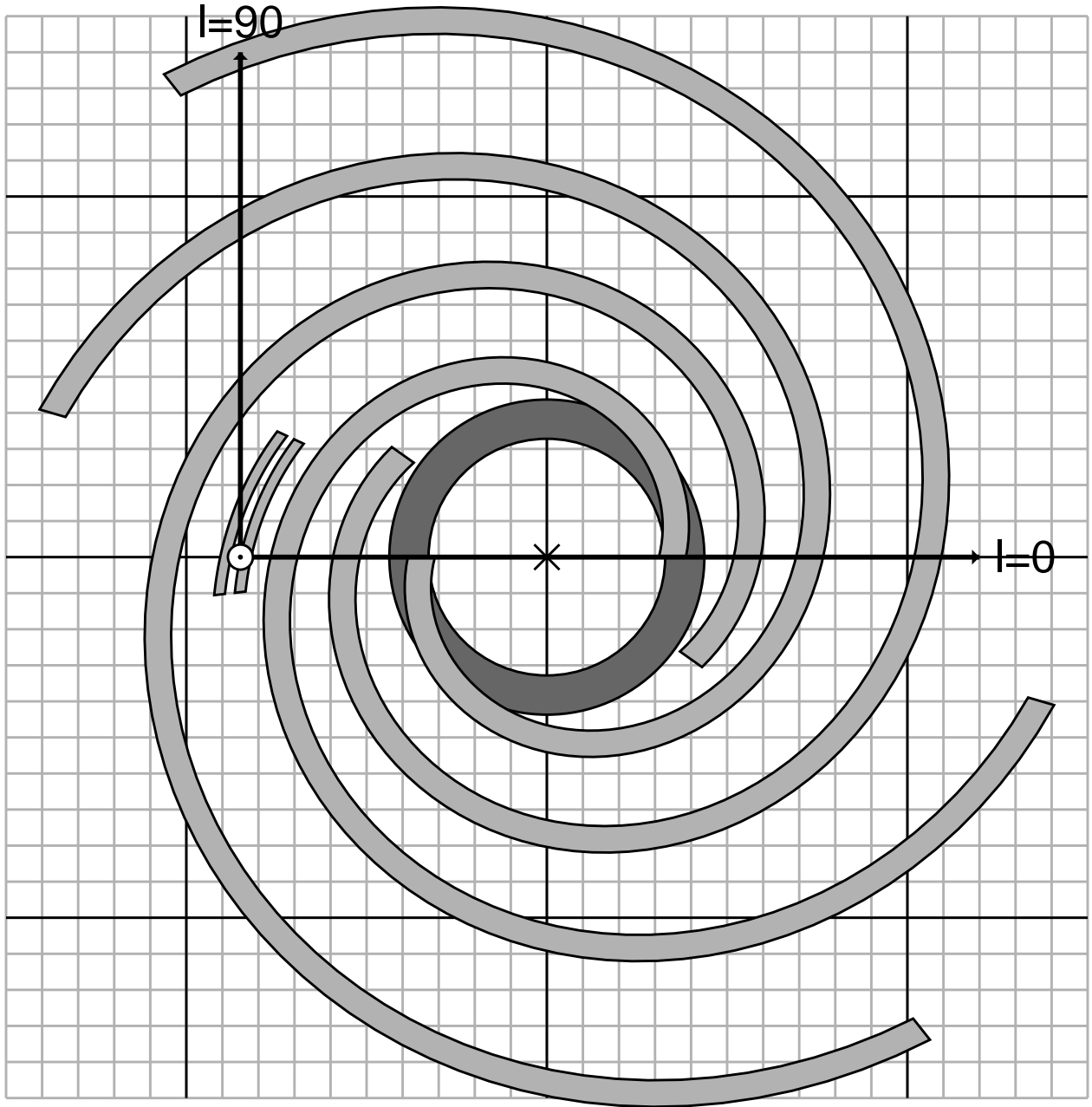


Fig. 1.— The pattern of spiral arms and the molecular ring in the starcount model. Each little square is 1 kpc wide.

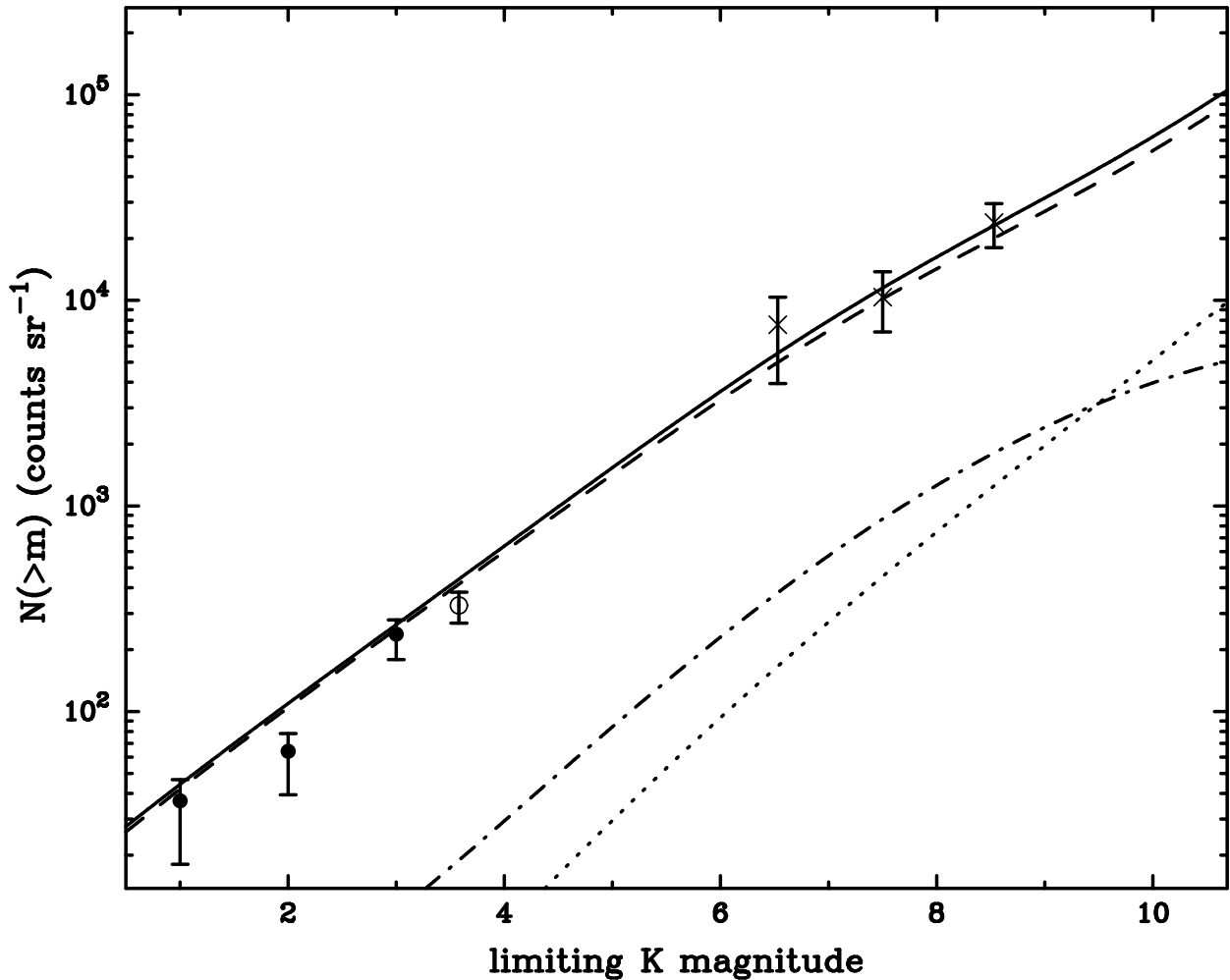


Fig. 2.— Comparison of model predictions with the observed cumulative star counts at the NGP (Elias 1978). The total counts (solid), disk component (dashed), spiral arm component (dot-dashed), and halo (dotted) are all shown. The dominance of the disk component which holds for $|b| \geq 20^\circ$ is readily apparent. The ring and bulge components are absent because of the high galactic latitude considered in this plot.

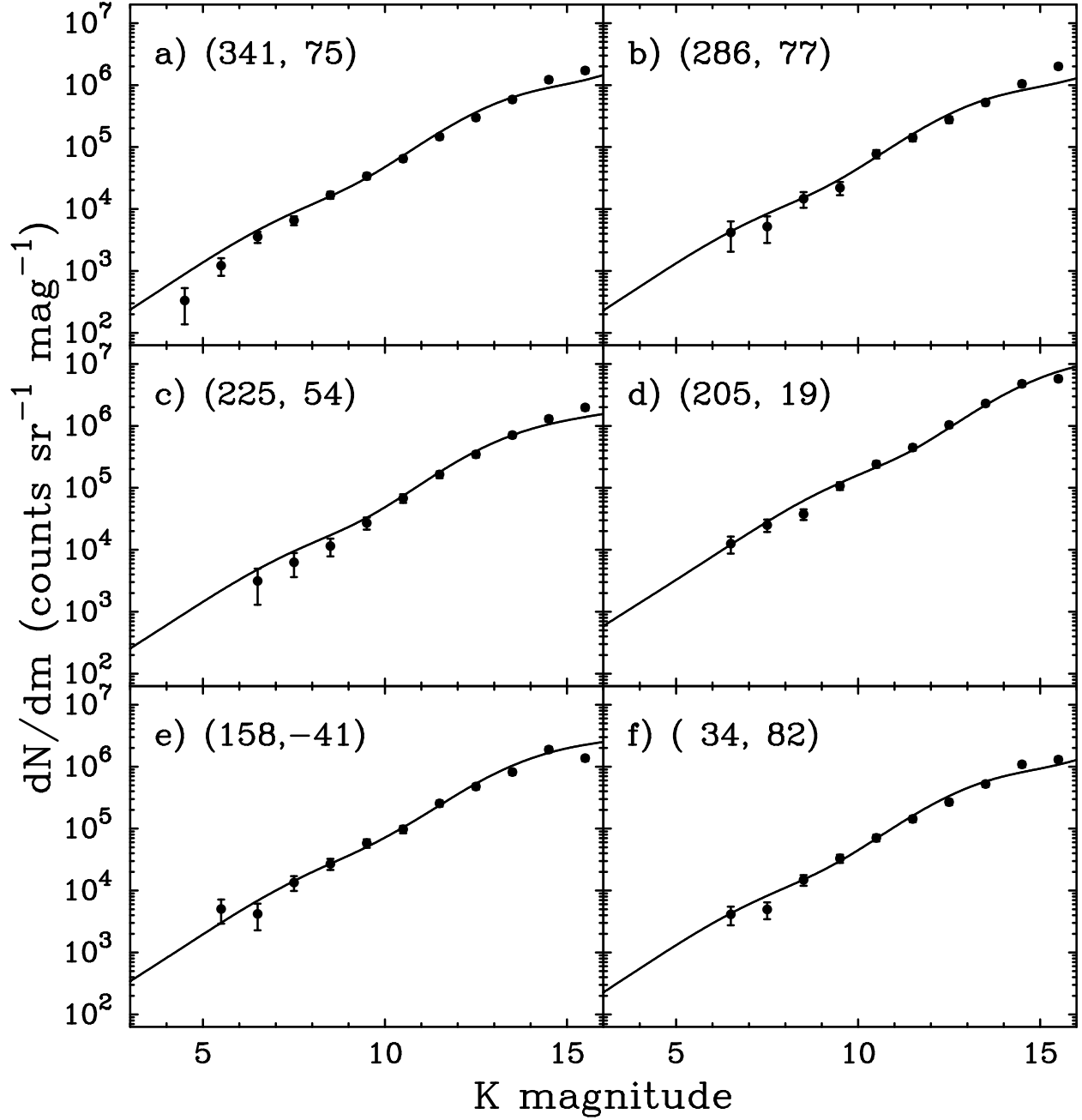


Fig. 3.— Comparison of the differential star counts from the 2MASS survey at $2.2 \mu\text{m}$ to the Cohen (1994) starcount model in six different fields. Galaxy counts become larger than the high b starcounts for $K \geq 15.5$ (Gardner, Cowie & Wainscoat 1993).

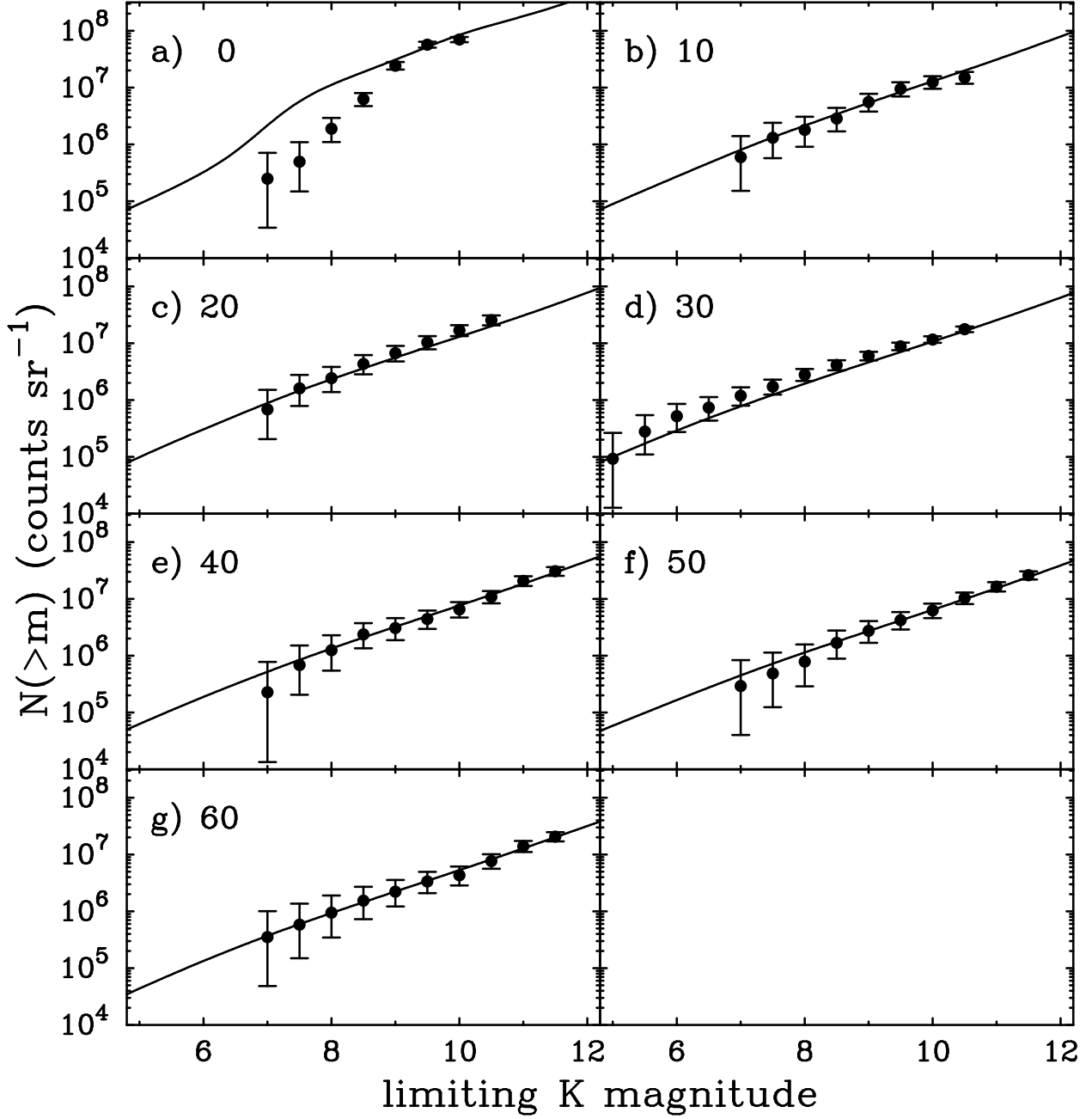


Fig. 4.— Comparison of the cumulative star counts in the galactic plane from EAG with the Cohen (1994) model star counts. The model is consistent with the data with the exception of the galactic center.

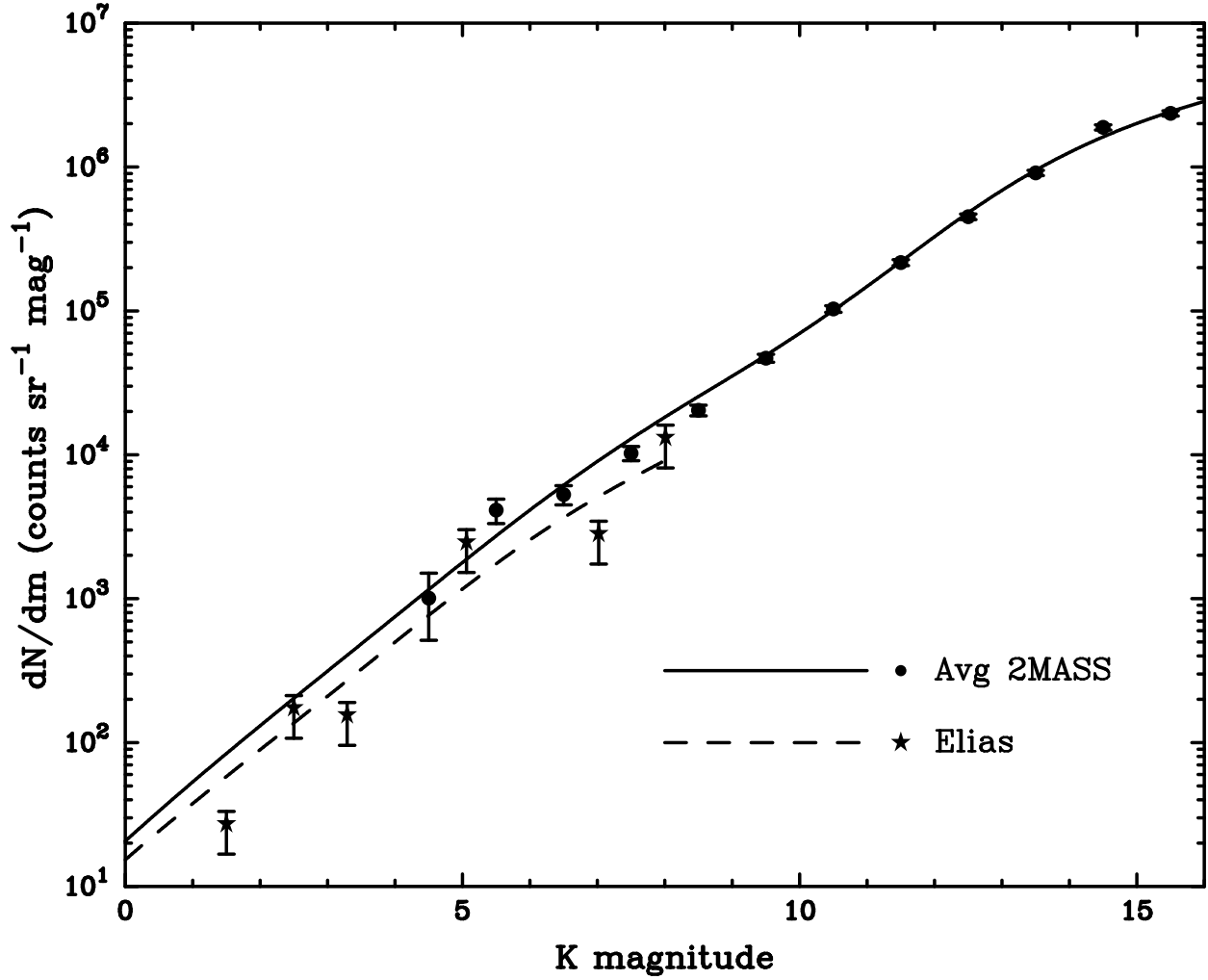


Fig. 5.— Comparison of the Cohen (1994) model counts with high galactic latitude observations over a wide range of magnitudes. The 2MASS points are the average of all 6 fields.

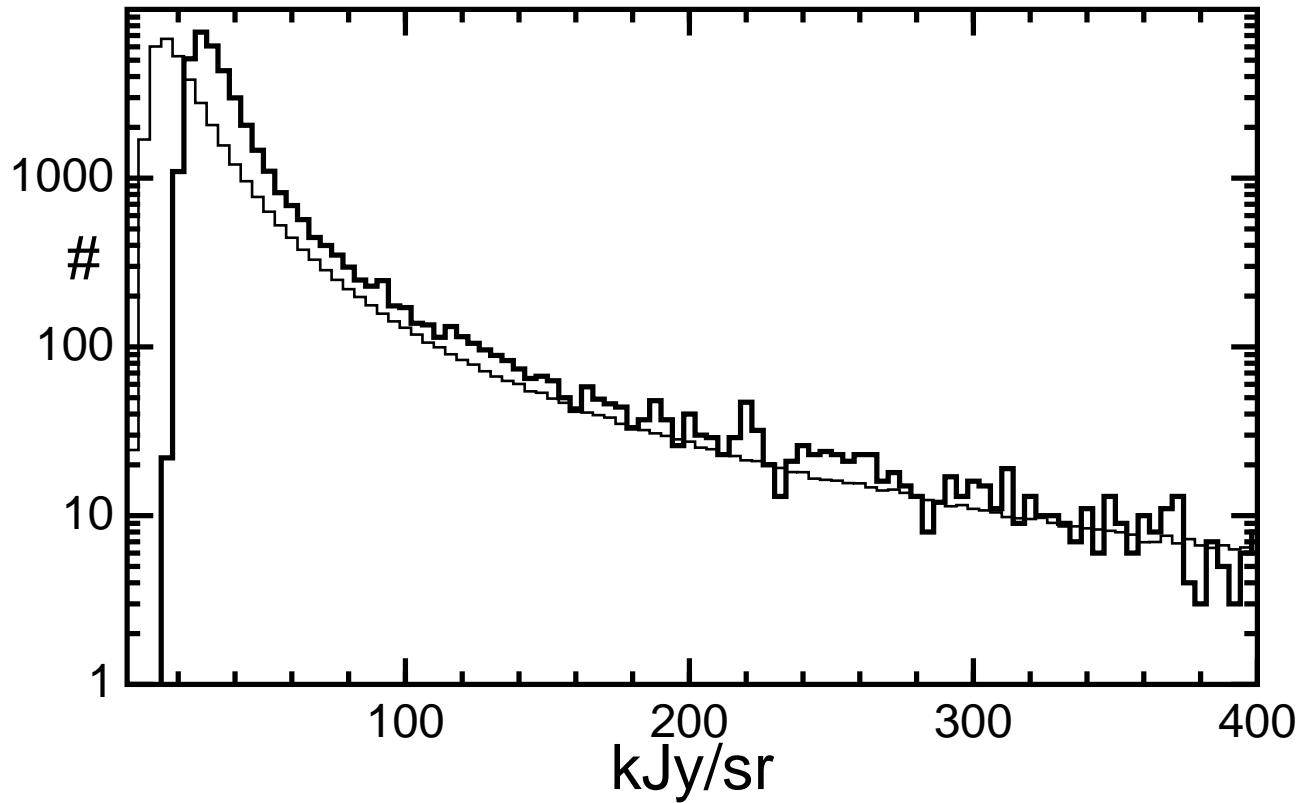


Fig. 6.— The DIRBE and model histograms of number of pixels receiving a given flux. The heavy line shows the real data for the region with $\sin|b| > 0.9$ at $3.5 \mu\text{m}$ while the thin line shows the predicted histogram computed for 100 times more pixels than the real data and scaled down by a factor of 100. The offset between the two histograms is the CIRB.

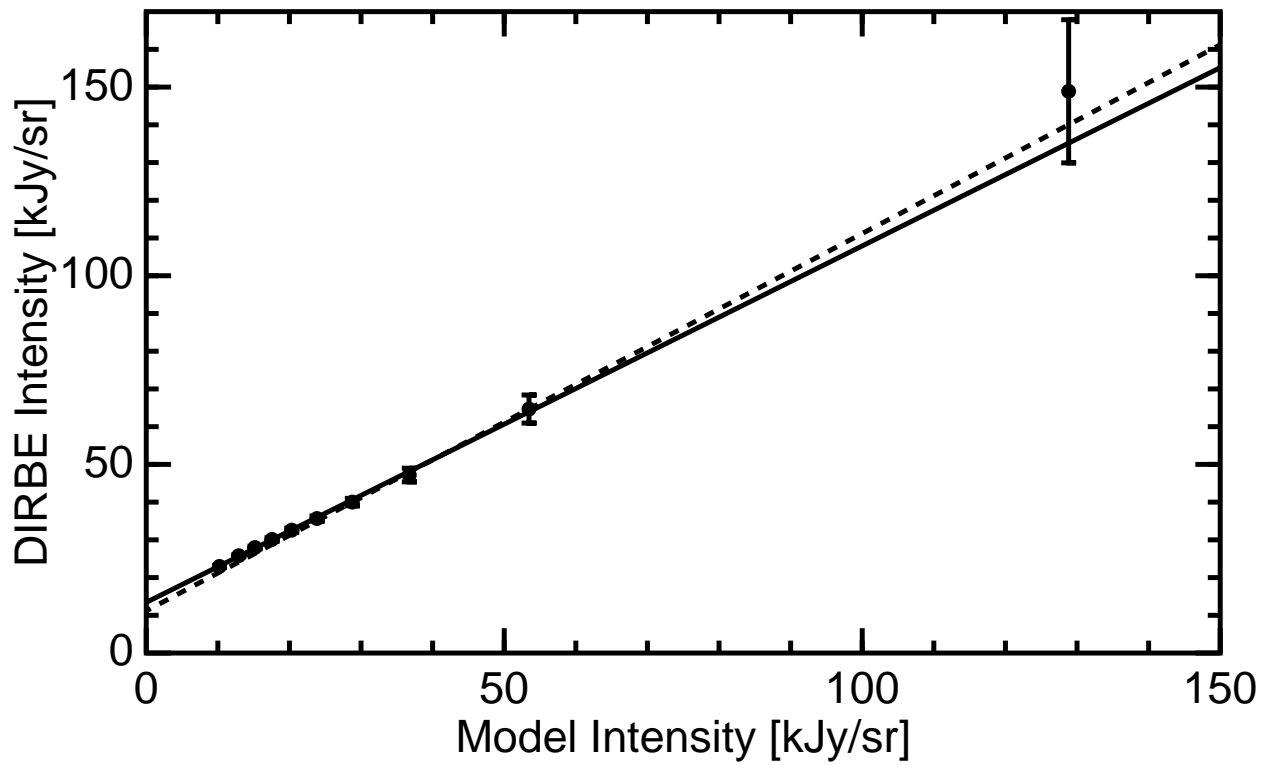


Fig. 7.— DIRBE and model histogram values at the 5^{th} , 15^{th} , \dots 95^{th} %-tiles for the region with $\sin|b| > 0.9$ at $3.5 \mu\text{m}$. Two fits are shown: one with the slope fixed to unity [dashed], and the second with the slope as a free parameter [solid].

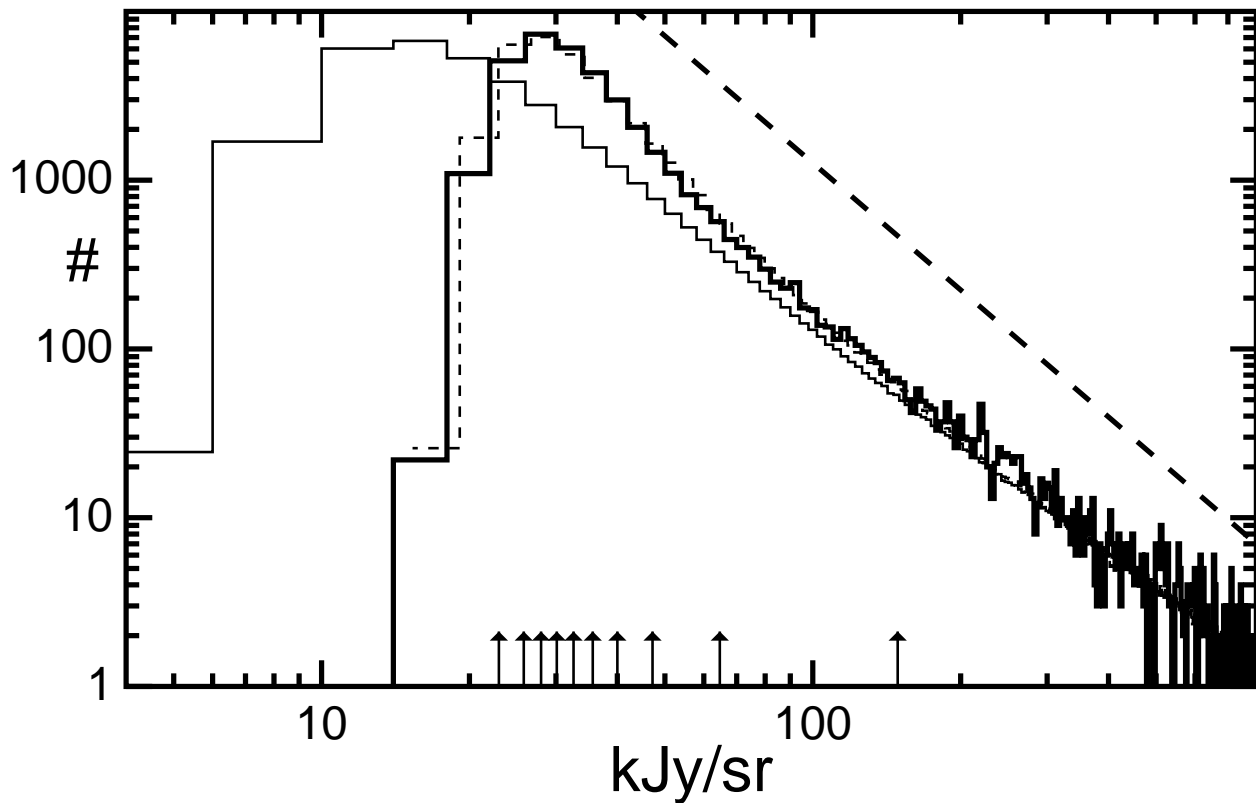


Fig. 8.— The DIRBE and model histograms of number of pixels receiving a given flux in the region with $\sin |b| > 0.9$ at $3.5 \mu\text{m}$. Both the original model histogram and the best fit with slope 0.9485 and intercept $13.42 \text{ kJy sr}^{-1}$ are shown. The arrows along the x-axis show the positions of the percentiles used in fitting. The dashed straight line with a slope of $-5/2$ shows a Euclidean source count.

$$I(3.5) - 0.4976 * I(2.2) - 0.00094 * I(100) + 0.0088$$

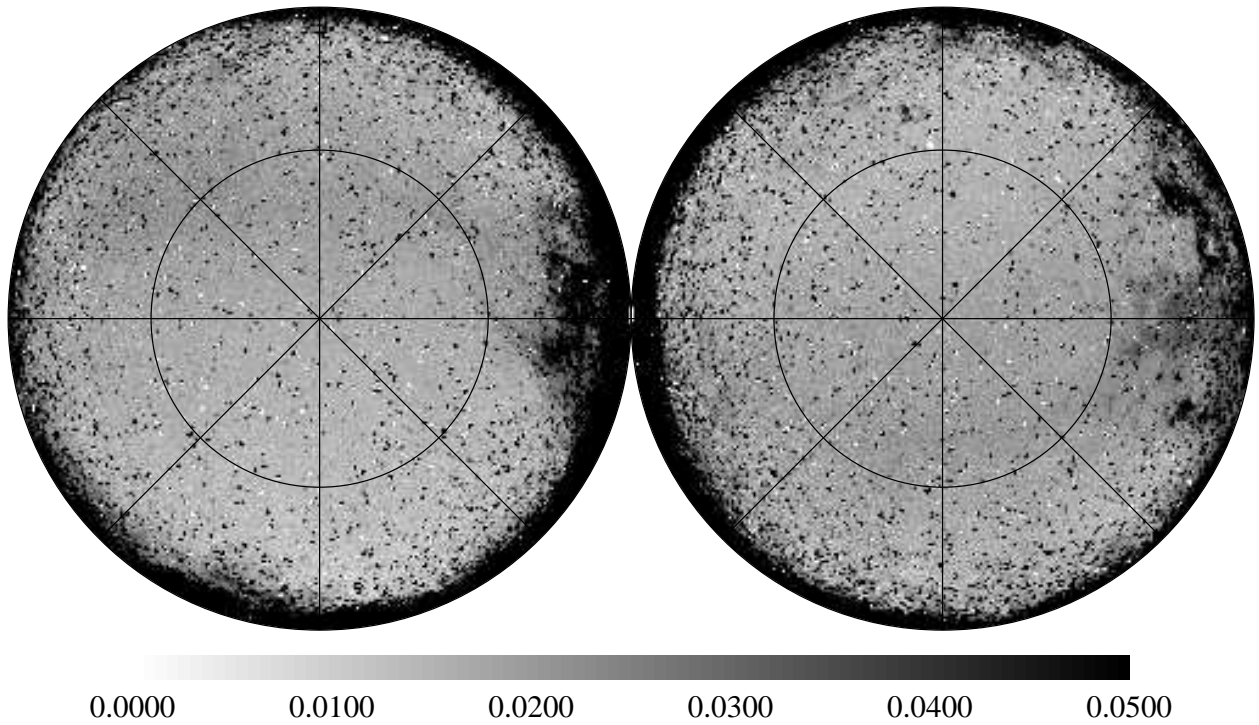


Fig. 9.— The residual at 3.5 μm after subtracting a fraction of the 2.2 μm map to remove stars and a fraction of the 100 μm map to remove ISM dust emission. $l = 0^\circ$ is at the center of the figure, $b = 90^\circ$ is the center of the left circle, and $l = 90^\circ$ is toward the bottom of both circles. Intensities are given in MJy sr^{-1} .

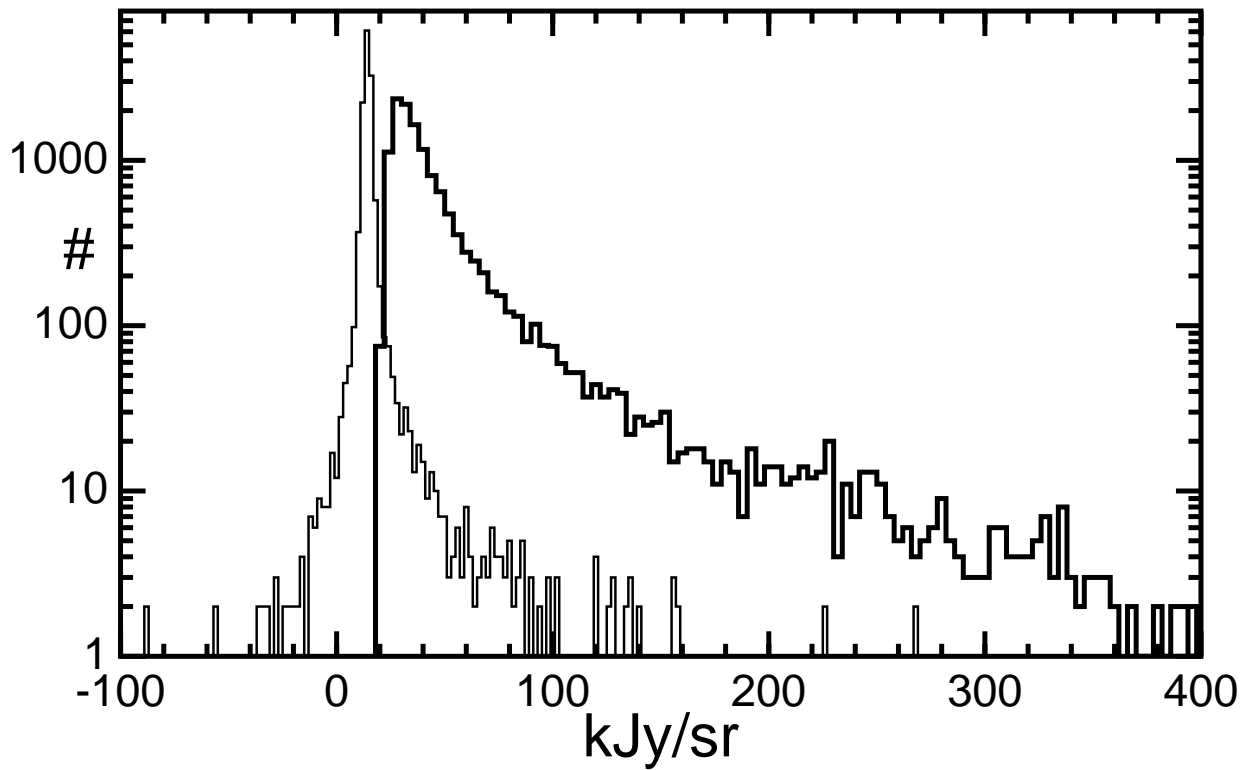


Fig. 10.— The histogram of the zodi-subtracted $3.5 \mu\text{m}$ map in the region with $b > 45^\circ$ and $\beta > 45^\circ$ (thick line) compared to the histogram of the residual map from Figure 9 in the same region (thin line).